crystals

MDPI

Article

Improvement of Mechanical Properties with Non-Equimolar CrNbTaVW High Entropy Alloy

Francisco Antão [1], Ricardo Martins [1], José Brito Correia [2], Rui Coelho da Silva [1], António Pereira Gonçalves [3], Elena Tejado [4], José Ygnacio Pastor [4], Eduardo Alves [1] and Marta Dias [1,*]

[1] Instituto de Plasmas e Fusão Nuclear, Instituto Superior Técnico, Universidade de Lisboa, Av. Rovisco Pais, 1049-001 Lisboa, Portugal; fantao@ctn.tecnico.ulisboa.pt (F.A.); ricardo.martins@ctn.tecnico.ulisboa.pt (R.M.); rmcs@ctn.tecnico.ulisboa.pt (R.C.d.S.); ealves@ctn.tecnico.ulisboa.pt (E.A.)
[2] LNEG, Laboratório Nacional de Energia e Geologia, Estrada do Paço do Lumiar, 1649-038 Lisboa, Portugal; brito.correia@lneg.pt
[3] C2TN, Instituto Superior Técnico, Universidade de Lisboa, Campus Tecnológico e Nuclear, Estrada Nacional 10, 2695-066 Bobadela, Portugal; apg@ctn.tecnico.ulisboa.pt
[4] Departamento de Ciencia de Materiales-CIME, ETSI Caminos, Canales y Puertos, Universidad Politécnica de Madrid, 28040 Madrid, Spain; elena.tejado@upm.es (E.T.); jy.pastor@upm.es (J.Y.P.)
* Correspondence: marta.dias@ctn.ist.utl.pt; Tel.: +351-219946000; Fax: +351-219550117

Abstract: $CrNbTaVW_x$ with (x = 1 and 1.7) high entropy alloys have been devised for thermal barriers between the plasma-facing tungsten tiles and the copper-based heat sink in the first wall of fusion nuclear reactors. These novel materials were prepared by ball milling and consolidated by Upgrade Field Assisted Sintering Technology at 1873 K under an applied pressure of 90 MPa for 10 min. In this work, the structural and mechanical properties of these materials were evaluated. Consolidated samples presented a major phase with a bcc-type structure with lattice parameter value of 0.316 nm for CrNbTaVW and $CrNbTaVW_{1.7}$ compositions. Moreover, observation of the microstructures evidences also two minor phases: Ta-Nb-Cr and Ta-V rich (in which carbon is detected). Despite the similarity in the structural properties of these two alloys, their mechanical properties are distinct. The flexural stress for the sample with higher amount of W ($CrNbTaVW_{1.7}$) is higher by 50% in the 298–873 K range, with an increased strain to fracture, which can be associated with reduced brittleness caused by the additional W incorporation.

Keywords: high entropy alloys; mechanical alloying; consolidation; microstructure; mechanical properties

Citation: Antão, F.; Martins, R.; Correia, J.B.; da Silva, R.C.; Gonçalves, A.P.; Tejado, E.; Pastor, J.Y.; Alves, E.; Dias, M. Improvement of Mechanical Properties with Non-Equimolar CrNbTaVW High Entropy Alloy. *Crystals* **2022**, *12*, 219. https://doi.org/10.3390/cryst12020219

Academic Editors: Rui Feng, Ke An and Peter K. Liaw

Received: 17 January 2022
Accepted: 28 January 2022
Published: 1 February 2022

1. Introduction

Tungsten is considered the best candidate for plasma facing tiles due to its endurance for high temperature and irradiation resilience and resistance, high melting point, low sputtering rate, and low tritium retention [1]. However, the currently available grades are brittle at temperatures below 623 K, due to the occurrence of a ductile-to-brittle transition in the range of 623 K to 873 K [2]. On the other hand, the material selected for heat sink behind the plasma-facing components is a CuCrZr alloy with a service temperature limited to ~623 K [3]. These two materials, W and CuCrZr alloy, thus show a large mismatch in working temperatures, demanding resourcefulness solutions for their joint operation. A possible solution is the introduction of a thermal barrier interlayer between these two components. One approach to solve this issue is the use of high entropy alloys compatible with both W and the CuCrZr alloys which can work as a thermal barrier interlayer capable of minimizing the thermal mismatch between both materials, keeping them in their required work temperature intervals.

High-entropy alloys (HEAs) are a class of materials developed in recent years which exhibit excellent properties for this application, such as high hardness [4], high thermal

stability [5], and low thermal diffusivity [5,6]. In general, HEAs usually possess unique microstructures and, consequently, different properties [7–10] that can be tuned according to the task envisaged. The use of HEAs based on refractory-elements (Mo, Nb, Ta, W, and V) was first introduced by Senkov et al. [11] mainly as candidates for structural applications at temperatures above 1373 K, but subsequent alloys have been drawn from a broader palette of nine elements in Group IV (Ti, Zr, and Hf), Group V (V, Nb, and Ta), and Group VI (Cr, Mo, and W). Many refractory HEAs were subsequently developed to obtain improved strength, room temperature ductility, and high hardness up to 1873 K. Despite the numerous studies on refractory HEAs, only a few recent works have been devoted to the high temperature class of alloys, with output on microstructure characterization and mechanical properties [10,11]. This research presents a study of the $CrNbTaVW_x$ high entropy alloys changing the W amount (x = 1 and 1.7), including its synthesis method and resulting microstructure together with its high temperature mechanical properties. Therefore, the study of the effect of the increasing W content, on the equiatomic CrNbTaVW in terms of structural and mechanical properties, is the goal of the present work.

2. Experimentals

The W, Cr, Ta, Nb, and V powders (AlfaAesar, nominal purity of 99.9% with average particle size of 10 μm) were mixed in two different proportions: equiatomic and non-equiatomic in a glove box and mechanically alloyed in a high-energy planetary ball mill, PM 400 MA, with WC balls and vials. The balls to powder mass ratio was 10:1, and the milling was carried out at 380 rpm for effective times up to 2 h. The samples and their respective designation are showed in Table 1.

Table 1. Atomic percentage of each element in all samples and the respective designation.

Samples $CrNbTaVW_x$	Designation	Cr (at.%)	Nb (at.%)	Ta (at.%)	V (at.%)	W (at.%)
x = 1 equiatomic	CrNbTaVW	20	20	20	20	20
x = 1.7 non-equiatomic	$CrNbTaVW_{1.7}$	17.5	17.5	17.5	17.5	30

The consolidation was performed in graphite dies of 10 mm diameter and 5 mm height by the Upgraded Field Assisted Sintering technology (U-FAST) process. A preliminary degassing step was conducted at 873 K for 2 min under a pressure of 15 MPa. The samples were then sealed under vacuum (5×10^{-3} Pa), at a temperature of 1873 K and an external hydrostatic pressure of 90 MPa was applied for 10 min and then allowed to cool to room temperature. The final discs produced have a volume of 0.63 cm^3 with an average weight of 6.86 g. After sintering, the apparent density was measured by the Archimedes method.

Powder X-ray diffraction (PXRD) was used to investigate the evolution of the powders mixtures before and after the 2 h milling. Measurements were made using a Philips X'Pert diffractometer in a Bragg-Brentano geometry with Cu K-alpha radiation, over a 2 range from 10° to 100° with a 2 step size of 0.03°. The consolidated samples were studied using a Bruker D8 AXS diffractometer in a grazing incidence geometry (GIXRD), with Cu K radiation incident at an angle of 3°, over 2 range from 20° to 90° with a 2θ step size of 0.02°. The ICDD database [12] was used for phase identification. The Powder Cell software package [13] was employed to simulate diffractograms for comparison with experimental data.

The metallographic preparation involved grinding with SiC paper and polishing with 6 μm, 3 μm, and 1 μm grade diamond suspensions. The microstructures were later observed in backscattered electron imaging (BSE) and secondary electron imaging (SE) modes using a JEOL JSM-7001F field emission gun scanning electron microscope (SEM) equipped with an Oxford Instruments X-ray EDS system. Quantitative analyses were

performed by energy dispersive spectrometry (EDS) of the X-rays emitted from the major phases present in the alloys. Each phase was analyzed in more than 10 randomly selected points. The EDS analyses were made in regions where the phases present extend over large areas in order to decrease the probability of spectral contamination or interference.

Thermodynamics calculations were performed to determine the possible structures formed in the sample, and to help with the interpretation and discussion of the results. Based on empirical models [8,14] using the enthalpies and entropies of mixing, ΔH_{mix} and ΔS_{mix}, the fractional atomic size differences δ and the valence electron concentrations, VEC, it is possible to predict the formation of solid solutions in the ranges $-15\,\text{kJ/mol} \leq \Delta H_{mix} \leq 5\,\text{kJ/mol}$, $0.01 \leq \delta \leq 0.06$, and $11\,\text{J/(K·mol)} \leq \Delta S_{mix} \leq 19.5\,\text{J/(K·mol)}$: the stable most phases are predicted to be fcc-type structure at VEC ≥ 8 and bcc-type structure at VEC < 6.87. Between these values, mixed fcc and bcc-type structures are expected to coexist. In this context, the calculations of the relevant properties of the CrNbTaVW and $CrNbTaVW_{1.7}$ high entropy alloys are presented in Table 2. Based on the calculated values, a predominance of bcc-type solid solutions is expected for both compositions.

Table 2. Thermodynamic calculations for the CrNbTaVW and $CrNbTaVW_{1.7}$ high entropy alloys.

Composition	ΔH_{mix} kJ/mol	ΔS_{mix} J/(K·mol)	$\delta \times 100$	VEC
CrNbTaVW	−5.28	13.38	5.09	5.4
$CrNbTaVW_{1.7}$	−5.35	13.15	4.48	5.48

Vickers microhardness was obtained by applying a load of 9.8 N for 15 s on an AKASHI MVK-EIII tester. Additionally, nanoindentation to a depth of 1500 nm was performed on the same samples using a standard Berkovich tip, calibrated using fused silica. The hardness measurements were performed on random regions. The average values of hardness and elastic modulus were taken from the unloading curve according to the Oliver and Pharr method [15]. Lastly, smooth bars of $0.8 \times 2\,\text{mm}^2$ sections were then cut by electro discharge machining for further mechanical testing. Quasi-static three-point bending (TPB) tests were then performed using 16 mm loading span at a constant cross head travel speed of 100 μm/min for easy control of the test process while obtaining accurate recording data. To investigate the flexural strength of these novel materials in their expected operating temperature range, TPB tests were performed at 298 K, 673 K, and 873 K under a high vacuum atmosphere (10^{-6} mbar). The flexural strength was later computed using Euler-Bernoulli equations for slender beams up to failure and their fracture surfaces were evaluated.

3. Results and Discussion

Figure 1a shows the X-ray pattern of the evolution of the CrNbTaVW alloy in three stages of synthesis: powder mixture of raw elements before milling, the as-milled powder (after 2 h milling), and the sintered sample. Comparing the diffractograms presented in (a) it is possible to observe that after 2 h of milling, the diffraction peaks of the individual elements can no longer be observed, and a set of broad peaks has developed. Moreover, weak peaks assigned to WC, are present in the diffractogram of the milled powder, which are attributed to the use of WC balls and vials as milling media. On the other hand, the diffractogram of the sintered sample evidences sharp peaks, which in agreement with Figure 1b correspond to a bcc-type structure with a lattice parameter 0.316 nm (observed already after 2 h milling as mentioned above) and another, minor phase (identified with the symbol * in Figure 1a with a lattice parameter of 0.334 nm) and the presence of small non-identified peaks. Note that the diffractogram of the sintered sample did not reveal the presence of WC as was observed in the milled powder. The experimental diffratogram of the $CrNbTaVW_{1.7}$ sample (Figure 1b) is very similar to the one presented for the equiatomic CrNbTaVW sample, with a major bcc-type structure phase with the same lattice parameter

of 0.316 nm. Due to the similarity of the two samples only the X-ray evolution for phase formation was shown for the equiatomic sample.

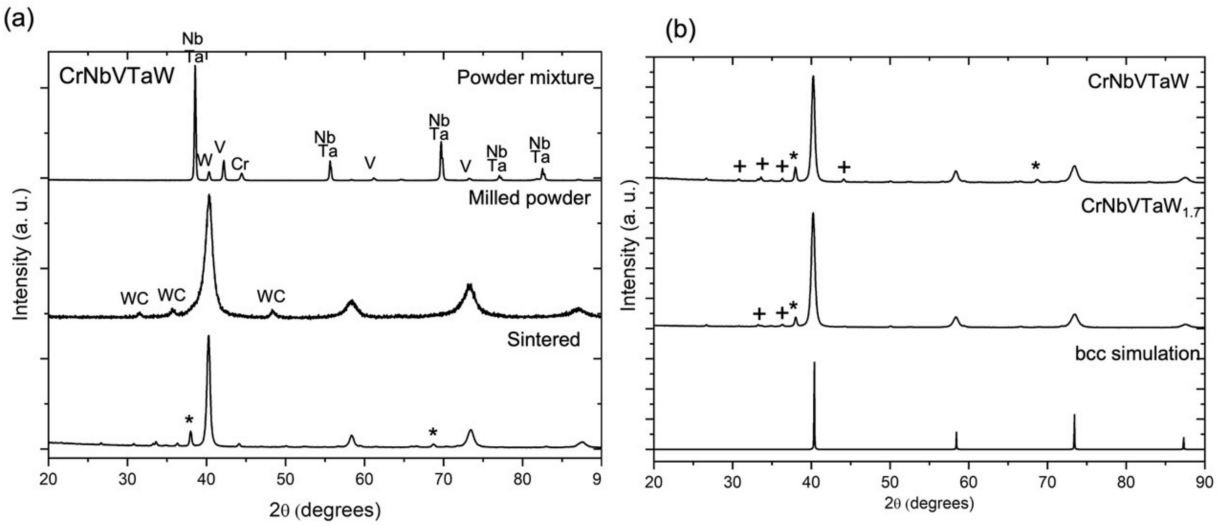

Figure 1. X-ray diffractogram of (**a**) evolution of the phase formation on CrNbTaVW high entropy alloy (powder mixture, milled powder and sintered sample) and (**b**) sintered CrNbTaVW and $CrNbTaVW_{1.7}$ together with theoretical simulation of the bcc-type structure with a = 0.316 nm. The symbol * indicates the presence of a bcc-type structure theoretical simulation with a = 0.334 nm. The symbols + indicate minor unidentified structures.

Figure 2 displays only the milled powder of CrNbTaVW (since the $CrNbTaVW_{1.7}$ powder is similar) and the microstructures of the sintered CrNbTaVW and $CrNbTaVW_{1.7}$ high entropy alloys. The milled powder of the CrNbTaVW sample exhibits a particle distribution with a size less than 10 microns and revealed the mixture of the elements. The microstructures of the sintered samples are similar and no extensive porosity (less than 5%) was observed in both samples, which is in agreement with the measured apparent density measured of 97% for CrNbTaVW and 95% for $CrNbTaVW_{1.7}$. Both microstructures revealed the presence of a major phase (indicated as a white arrow in Figure 2b,c) and two uniformly dispersed dark phases, located in the boundaries of the submicron matrix grains (indicated as a black arrow in Figure 2b,c). The EDS for the major phase for both compositions is evidenced in Table 3. The major phase for the equiatomic CrNbTaVW has a near equiatomic composition, however with less chromium and niobium while for the non-equiatomic $CrNbTaVW_{1.7}$ exhibits a near initial composition, however with more chromium and less niobium. Moreover, the grain size of the major phase is around 2 μm while for the dark phases is less than 1 μm. In fact, the contribution of the dark phases is minor compared to the major phase.

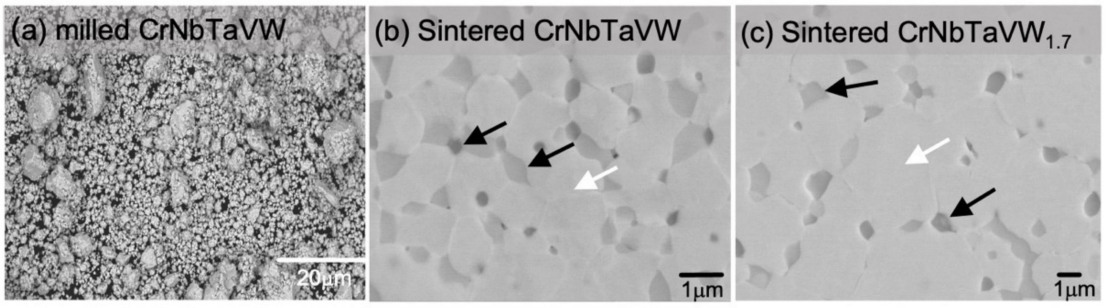

Figure 2. (**a**) BSE image of the milled powder of CrNbTaVW composition and microstructures of sintered (**b**) CrNbTaVW and (**c**) $CrNbTaVW_{1.7}$ high entropy alloys. The white arrows in (**b**,**c**) indicate the presence of the major phase. The black arrows in (**b**,**c**) indicate the presence of the dark phases.

Table 3. Average elemental composition on the major phase obtained by EDS analysis for both CrNbTaVW and $CrNbTaVW_{1.7}$ compositions.

Composition		W at.%	Ta at.%	Cr at.%	Nb at.%	V at.%
CrNbTaVW	EDS	23.52 ± 0.59	19.19 ± 0.76	20.42 ± 0.68	15.90 ± 0.47	20.97 ± 0.40
	Nominal	20	20	20	20	20
$CrNbTaVW_{1.7}$	EDS	30.59 ± 0.32	16.56 ± 0.27	19.88 ± 0.32	14.26 ± 0.14	18.70 ± 0.18
	Nominal	30	17.5	17.5	17.5	17.5

Figure 3a–f shows the EDS map of the regions found on the microstructure of the sintered CrNbTaVW high entropy alloy. The microstructure shows the presence of a major phase, as discussed above, and two darker regions (which indicate that they are richer in light elements) which correspond to a Ta-Nb-Cr and Ta-V richer. Since regions Ta-V rich are darker when compared to the other phases, an EDS spectrum at low energy of this region is shown in Figure 3g in order to distinguish light elements. In fact, the spectrum revealed a high intensity peak of C and O, which can explain the lower atomic number of this phase and consequently the presence of a dark phase. This result is in agreement with what was observed in the XRD between the diffractogram of the milled powder and the sintered sample; the WC was only observed in the milled powder which can probably indicate that the carbon diffused and formed phases in the consolidated sample. Moreover, the origin of this diffusion could be also the graphite molds using during the consolidation stages [14,16]. Consistent with the XRD results, the major phase identified in the microstructure should have a bcc-type structure with a lattice parameter of 0.3156 nm for both compositions.

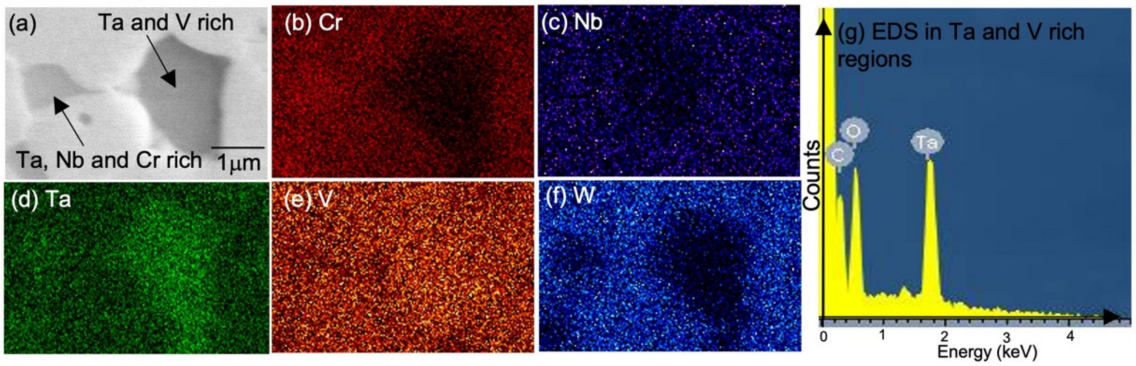

Figure 3. (**a**) SE image of the CrNbTaVW microstructure and the corresponding EDS maps for the (**b**) Cr-Lalpha, (**c**) Nb-Lalpha, (**d**) Ta-Lalpha, (**e**) V-Lalpha, (**f**) W-Lalpha and (**g**) EDS spectrum for regions rich in Ta and V.

Table 4 shows the hardness and the elastic modulus measured for consolidated CrNbTaVW and $CrNbTaVW_{1.7}$ high entropy alloys. The indentation hardness of the equiatomic composition was measured to be 19 GPa, whereas that of the non-equiatomic one was 17.5 GPa, this difference was also observed for the microscopic indentations (1380 and 1240, respectively). The relative small error bounds are attributed to the homogeneous microstructures. The equiatomic CrNbTaVW sample, as illustrated in Figure 2b, presented a much refined microstructure than that of $CrNbTaVW_{1.7}$, which implies a size-dependent strengthening behavior described by the Hall–Petch relationship. Since CrNbTaVW presents a smaller grain size, the required stress to pass dislocations across grain boundaries in crystal materials increases and therefore increases hardness.

Furthermore, the exhibited hardness results for both samples are considerably higher than those reported for other HEAs with similar compositions (mostly in general in the range 140 HV to 900 HV). Even though refractory metals present strong atomic bonding and hard crystal structures, HEAs are strengthened by significant lattice distortion (i.e.,

solid-solution hardening) [17]. On the other hand, the elastic modulus of the alloys obtained via nano-indentation are lower than the one for pure tungsten (400 GPa) but considerably higher than that of pure vanadium or niobium (128 GPa and 103 GPa, respectively) [18]. These results may be associated with the extensive solid solution formation between the constituents, which improves the ductility and strength of the alloys over non-alloyed metals [19].

Table 4. Hardness and Elastic modulus for both compositions CrNbTaVW and $CrNbTaVW_{1.7}$.

Composition	Hardness Vickers	Hardness Nano (GPa)	Elastic Modulus
CrNbTaVW	1380 ± 40	19.0 ± 0.7	329 ± 7
$CrNbTaVW_{1.7}$	1240 ± 20	17.5 ± 0.3	316 ± 4

The results of the three-point bending test are presented in Figure 4a,b, with the representative loading curves at each testing temperature (298 K, 673 K, and 873 K) for both compositions. Both alloys show a linear elastic behavior up to fracture in all the temperature range, which indicates that the material is brittle in the temperature chosen. However, the graphs show (Figure 4a,b) that the strain percentage and the stress achieved for the non-equiatomic $CrNbTaVW_{1.7}$ is higher than the equiatomic CrNbTaVW sample. Moreover, Figure 4c exhibits the flexural stress as a function of the testing temperatures for the CrNbTaVW and $CrNbTaVW_{1.7}$ compositions. At 673 K and 873 K the measured flexural strengths are higher than at 298 K, for both compositions. This fact may be attributed to the approach of the ductile-to-brittle transition temperature typical of the bcc-type structures, such as that of tungsten, a constituent of the alloy, at ~623 K [20], which promotes a more extensive deformation, and the superior flexural strength of the system. In addition, the results show that the flexural strength for the sample with higher amount of W (more 10 at.%) is higher with an increase of 50%. This improvement of the strength was also addressed by Wu et al. [21] and it was primarily associated with the solid solution hardening caused by the W incorporation. The hardening effect of W additions in the studied alloys can be explained in terms of the variation of the interatomic spacing with the increased number of W atoms, which promotes a severely distorted crystal lattice. Traditional solid solution strengthening theory [22] suggests that solute atoms with large lattice and modulus mismatch with the "solvent" could be the ideal intrinsic strengthener. Among the transitional metals, W exhibits both large lattice and modulus differences from those of Cr, Nb, V, and, to a minor extent, Ta and thus it leads to significant short-range bending/curving of the dislocations which consequently require elevated stress to move these dislocations.

Despite the improvement of the mechanical properties with the increasing of W amount, the materials are brittle in the regime studied. This lack of ductility of the refractory high entropy alloys in the low-temperature regime (below 873 K) was previously addressed by Senkov et al. [23] and in fact their compressive ductility is indeed limited. Furthermore, HEAs with similar compositions, NbMoTaW and NbMoTaVW, showed only yield strength above 1873 K [23] and, in fact, only those refractory HEAs of the TiZrHfNbTa system showed some tensile ductility at low temperatures [24]. However, the increased strength observed at temperatures close to the expected temperature window (573–823 K estimated by T. R. Barrett in [25]) of the thermal barrier, it seems not to be enough for the expected application.

After the three-point bending tests, every fracture surface was analyzed by SEM and the corresponding micrographs are presented in Figure 5 for both samples. The CrNbTaVW sample exhibits a fracture surface formed at 298 K with both intergranular (between-grains) (Figure 5a) and transgranular (through-grain) fracture (Figure 5b), the latter observed exclusively in larger-sized particles and identified by bright crystalline cleavage facets with ridge patterns. These large particles were identified as Ta-rich phases, as observed in Figure 6, and could be indeed the origin of the fracture since its size (several microns)

was indeed too large to strengthen the alloy by precipitation hardening. The presence of these microstructural defects, as well as the lower content of W in the HEA lattice, could be the reason why, despite presenting a more refined microstructure, the mechanical strength of this alloy is considerably lower. The transgranular fracture was less common but was also observed in samples tested at 873 K, as some residual cleavage facets (transgranular fracture produced along the crystalline planes) were still found (Figure 5c,d). Intergranular fracture caused by grain boundary decohesion took place and was indeed observed for all temperatures.

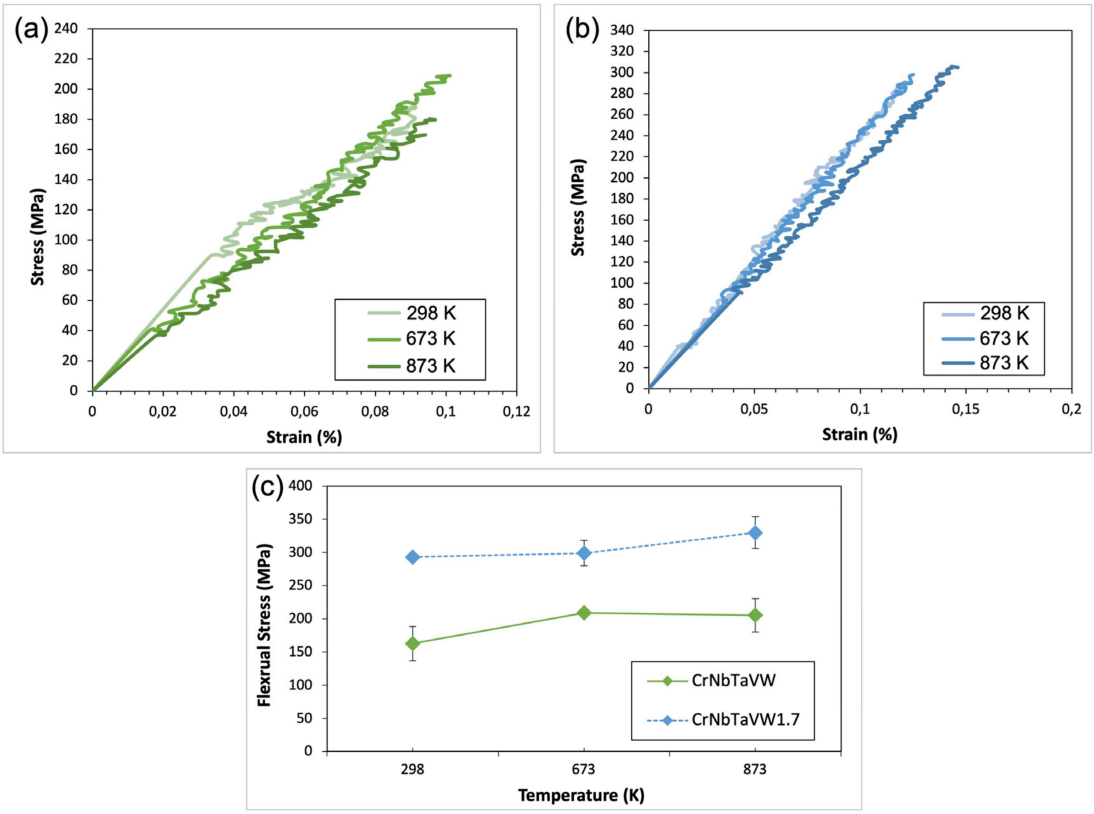

Figure 4. Stress-strain curves for (**a**) CrNbTaVW and (**b**) $CrNbTaVW_{1.7}$ and (**c**) flexural strength-fracture strain of both samples at 298 K, 673 K and 873 K.

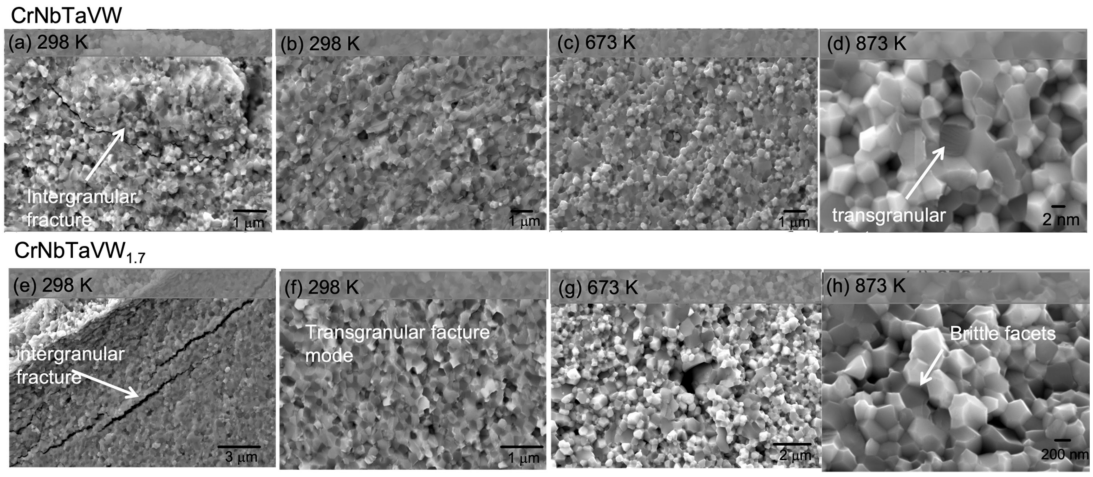

Figure 5. Types of fracture and cleavage facets observed throughout the three test temperatures for CrNbTaVW at (**a**) and (**b**) 298 K, (**c**) 673 K and (**d**) 873 K and for $CrNbTaVW_{1.7}$ at at (**e**) and (**f**) 298 K, (**g**) 673 K and (**h**) 873 K.

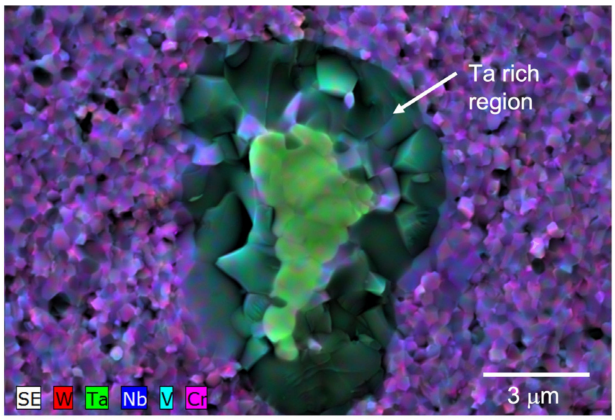

Figure 6. EDS compositional mapping of the Ta-enriched phases in the fracture surface of CrNbTaVW high entropy alloy.

As observed for CrNbTaVW, three-point bending tests showed macroscopic linear elastic fracture behavior in all the temperature range, from 273 K to 873 K for the $CrNbTaVW_{1.7}$ sample. On the local scale, fracture surfaces revealed a predominantly intergranular fracture at room temperature (Figure 5e). At higher temperatures, also mostly intergranular fracture modes were observed, although again, residual cleavage facets can still be observed in some grains. However, no Ta-rich large particles were detected on the fractured surfaces when compared with the equiatomic CrNbTaVW which point to the high mechanical strength of this alloy.

It has been reported that non-equiatomic HEA compositions present improved mechanical properties [26]. This has been ascribed to the activation of a combination of different strengthening mechanisms but a major feature is that deviating from the equiatomic composition allows avoiding brittle intermetallic phases. This approach has been used for HEAs for fusion application [16] where a reduction of hardness via increase of W content translates into enhanced ductility. In the present materials there is no evidence of equiaxed dimples, associated with shear deformation and high fracture toughness, usually seen only in fcc-structure type HEA [27]. In bcc-structure type HEA cleavage provides a moderate degree of toughness but these alloys are in general more brittle than those of fcc-structure type structure. In general porosity in sintered materials is also detrimental for mechanical properties [28], the ratio of about 0.7 between macrohardness and microhardness is lower than expected with the measured densification 97%–95%, hinting at an additional brittleness mechanism. The segregation of brittle intermetallic phases at grain boundaries have been identified as detrimental to the fracture resistance of HEAs [27]. It was demonstrated that single crystal fail by quasi-cleavage fracture with high fracture toughness even with bcc-type structure HEAs [29]. In summary, this study of CrNbTaVW and $CrNbTaVW_{1.7}$ high entropy alloys evidences the relative brittleness of bcc-type structure HEAs, but indicates potential enhancement of mechanical behavior for such materials, via non-equiatomic compositions, enabling a lower hardness of the major phase, as well as to pinpoint general trends and thus suggest future research directions in this field.

4. Conclusions

In the present study, a novel CrNbTaVW and $CrNbTaVW_{1.7}$ high entropy alloys were successfully synthesized by a combination of mechanical alloying and ultra-fast field-assisted sintering technique. Both samples are very similar from the structural point of view, since both presented a major bcc (a = 0.316 nm) with a multiphasic microstructure. Mechanical properties show that both materials are brittle at the temperatures studied (298 K, 673 K and 873 K). However, an improvement in flexural strength and strain to fracture was observed in the sample with a higher amount of W, which is an indication of enhanced toughness due to the addition of W. As a conclusion, the characterization

of the $CrNbTaVW_x$ high entropy alloys revealed that these materials are brittle in the temperature ranges studied, however the potential enhancement of mechanical behavior for such materials, via non-equiatomic compositions suggests an open door for future research.

Author Contributions: Conceptualization, F.A., R.M., J.B.C. and M.D.; methodology, F.A., M.D., A.P.G., E.T. and J.Y.P.; software, R.C.d.S.; validation, E.A. and M.D.; formal analysis, E.A. and M.D.; investigation, F.A. and M.D.; resources, E.A.; data curation, R.C.d.S.; writing—F.A. and M.D.; writing—review and editing, M.D.; visualization, M.D.; supervision, M.D.; project administration, M.D.; funding acquisition, E.A. All authors have read and agreed to the published version of the manuscript.

Funding: IPFN activities received financial support from "Fundação para a Ciência e Tecnologia" through projects UIDB/50010/2020 and UIDP/50010/2020. The Spanish authors would also like to acknowledge the Ministerio de Economía y Competitividad of Spain 35 (MAT2015-70780-C4-4-P and PID2019-106631GB-C44), the Comunidad de Madrid (S2018/NMT-36 4411ADITIMAT-CM) and, especially, the Universidad Politécnica de Madrid in the line of action for encouraging research from young doctors throught the project M190020074EMTG, COAT4FUSION.

Institutional Review Board Statement: Not applicable.

Informed Consent Statement: Not applicable.

Conflicts of Interest: The authors declare no conflict of interest.

References

1. Baluc, N.; Abe, K.; Boutard, J.; Chernov, V.; Diegele, E.; Jitsukawa, S.; Kimura, A.; Klueh, R.; Kohyama, A.; Kurtz, R.; et al. Status of R & D activities on materials for fusion power reactors. *Nucl. Fusion.* **2007**, *47*, S696–S717.
2. Gumbsch, P. Brittle fracture and the brittle-to-ductile transition of tungsten. *J. Nucl. Mater.* **2003**, *323*, 304–312. [CrossRef]
3. Stork, D.; Agostini, P.; Boutard, J.; Buckthorpe, D.; Diegele, E.; Dudarev, S.; English, C.; Federici, G.; Gilbert, M.; Gonzalez, S.; et al. Developing structural, high-heat flux and plasma facing materials for a near-term DEMO fusion power plant: The EU assessment. *J. Nucl. Mater.* **2014**, *455*, 277–291. [CrossRef]
4. Tong, C.-J.; Chen, M.-R.; Yeh, J.-W.; Lin, S.-J.; Chen, S.-K.; Shun, T.-T.; Chang, S.Y. Mechanical performance of the Al x CoCrCuFeNi high-entropy alloy system with multiprincipal elements. *Metall. Mater. Trans. A* **2005**, *36*, 1263–1271. [CrossRef]
5. Tsai, M.-H.; Wang, C.-W.; Tsai, C.-W.; Shen, W.-J.; Yeh, J.-W.; Gan, J.-Y.; Wu, W.-W. Thermal Stability and Performance of NbSiTaTiZr High-Entropy Alloy Barrier for Copper Metallization. *J. Electrochem. Soc.* **2011**, *158*, H1161. [CrossRef]
6. Lu, C.-L.; Lu, S.-Y.; Yeh, J.-W.; Hsu, W.-K. Thermal expansion and enhanced heat transfer in high-entropy alloys. *J. Appl. Cryst.* **2013**, *46*, 736–739. [CrossRef]
7. Zhou, Y.; Lu, Z.; Zhan, M. An investigation of the erosion-corrosion characteristics of ductile cast iron. *Mater. Des.* **2007**, *28*, 260–265. [CrossRef]
8. Guo, S.; Liu, C.T. Phase stability in high entropy alloys: Formation of solid-solution phase or amorphous phase. *Prog. Nat. Sci. Mater. Int.* **2011**, *21*, 433–446. [CrossRef]
9. Otto, F.; Dlouhý, A.; Somsen, C.; Bei, H.; Eggeler, G.; George, E.P. The influences of temperature and microstructure on the tensile properties of a CoCrFeMnNi high-entropy alloy. *Acta Mater.* **2013**, *61*, 5743–5755. [CrossRef]
10. Senkov, O.N.; Woodward, C.; Miracle, D.B. Microstructure and Properties of Aluminum-Containing Refractory High-Entropy Alloys. *Jom* **2014**, *66*, 2030–2042. [CrossRef]
11. Senkov, O.N.; Miracle, D.B.; Chaput, K.J.; Couzinie, J.-P. Development and exploration of refractory high entropy alloys—A review. *J. Mater. Res.* **2018**, *33*, 3092–3128. [CrossRef]
12. The International Centre for Diffraction Data-ICDD. Available online: http://www.icdd.com/ (accessed on 23 April 2020).
13. BAM Berlin PowderCell. Available online: http://www.ccp14.ac.uk/ccp/web-mirrors/powdcell/a_v/v_1/powder/e_cell.html (accessed on 23 April 2020).
14. Zhang, Y.; Zhou, Y.J.; Lin, J.P.; Chen, G.L.; Liaw, P.K. Solid-solution phase formation rules for multi-component alloys. *Adv. Eng. Mater.* **2008**, *10*, 534–538. [CrossRef]
15. Oliver, W.C.; Pharr, G.M. An improved technique for determining hardness and elastic modulus using load and displacement sensing indentation experiments. *J. Mater. Res.* **1992**, *7*, 1564–1583. [CrossRef]
16. Waseem, O.A.; Ryu, H.J. Powder Metallurgy Processing of a W_xTaTiVCr High-Entropy Alloy and Its Derivative Alloys for Fusion Material Applications. *Sci. Rep.* **2017**, *7*, 1926. [CrossRef] [PubMed]
17. Kim, H.; Nam, S.; Roh, A.; Son, M.; Ham, M.-H.; Kim, J.-H.; Choi, H. Mechanical and electrical properties of NbMoTaW refractory high-entropy alloy thin films. *Int. J. Refract. Met. Hard Mater.* **2019**, *80*, 286–291. [CrossRef]
18. ASMIH Committee. *ASM Handbook: Properties and Selection*; ASM International: Almere, The Netherlands, 1990.

19. Senkov, O.N.; Scott, J.M.; Senkova, S.V.; Miracle, D.B.; Woodward, C.F. Microstructure and room temperature properties of a high-entropy TaNbHfZrTi alloy. *J. Alloys Compd.* **2011**, *509*, 6043–6048. [CrossRef]
20. Stephens, J.R. Review of Deformation Behavior of Tungsten At Temperatures Less Than 0.2 Absolute Melting Temperature. In *Nasa Tm X-2482*; National Aeronautics and Space Administration: Washington, DC, USA, 1972.
21. Wu, Z.; Guo, W.; Jin, K.; Poplawsky, J.D.; Gao, Y.; Bei, H. Enhanced Strength and Ductility of a Tungsten-doped CoCrNi Medium Entropy Alloy. *J. Mater. Res.* **2018**, *33*, 3301–3309. [CrossRef]
22. Rate Processes in Plastic Deformation of Materials: Proceedings from the Google Books. Available online: https://books.google.pt/books/about/Rate_Processes_in_Plastic_Deformation_of.html?id=tXsMYAAACAAJ&redir_esc=y (accessed on 3 January 2022).
23. Senkov, O.N.; Wilks, G.B.; Scott, J.M.; Miracle, D.B. Mechanical properties of Nb25Mo25Ta25W25 and V20Nb20Mo20Ta20W20 refractory high entropy alloys. *Intermetallics* **2011**, *19*, 698–706. [CrossRef]
24. Senkov, O.N.; Pilchak, A.L.; Semiatin, S.L. Effect of Cold Deformation and Annealing on the Microstructure and Tensile Properties of a HfNbTaTiZr Refractory High Entropy Alloy. *Metall. Mater. Trans. A* **2018**, *49*, 2876–2892. [CrossRef]
25. Barrett, T.; McIntosh, S.; Fursdon, M.; Hancock, D.; Timmis, W.; Coleman, M.; Rieth, M.; Reiser, J. Enhancing the DEMO divertor target by interlayer engineering. *Fusion Eng. Des.* **2015**, *98–99*, 1216–1220. [CrossRef]
26. Li, D.; Raabe, Z. Strong and Ductile Non-equiatomic High-Entropy Alloys 2017.pdf. *J. Met.* **2017**, *69*, 2099–2106.
27. Li, W.; Liaw, P.K.; Gao, Y. Fracture resistance of high entropy alloys: A review. *Intermetallics* **2018**, *99*, 69–83. [CrossRef]
28. Ternero, F.; Rosa, L.G.; Urban, P.; Montes, J.M.; Cuevas, F.G. Influence of the total porosity on the properties of sintered materials—A review. *Metals* **2021**, *11*, 730. [CrossRef]
29. Zou, Y.; Okle, P.; Yu, H.; Sumigawa, T.; Kitamura, T.; Maiti, S.; Steurer, W.; Spolenak, R. Fracture properties of a refractory high-entropy alloy: In situ micro-cantilever and atom probe tomography studies. *Scr. Mater.* **2017**, *128*, 95–99. [CrossRef]